HOSTED BY
ELSEVIER
Available online at www.sciencedirect.com
ScienceDirect
Soils and Foundations 62 (2022) 101222
www.elsevier.com/locate/sandf

Technical Paper

Anchor plate bearing capacity in flexible mesh facings

Antonio Pol [a,b,*], Fabio Gabrieli [a]

[a] Dept. ICEA, Universitá degli Studi di Padova, via Ognissanti 39, 35129, Italy
[b] MAST/GPEM, Université Gustave Eiffel, Bouguenais F-44344, France

Received 4 March 2022; received in revised form 25 August 2022; accepted 11 September 2022
Available online 8 October 2022

Abstract

This work addresses the problem of the loading capacity of an anchor plate coupled with a steel wire mesh in soil retaining applications. The interaction mechanism between the flexible mesh facing, the underlying soil layer and the plate is studied starting from the results of several laboratory punch tests involving both the plate and the mesh only, and the whole soil-mesh-plate system. The experimental tests have been reproduced by adopting a 3D discrete element model where also the wire mesh is discretized as an assembly of interconnected nodal particles. The interaction between these particles is ruled by elasto-plastic tensile force–displacement laws in which a distortion is introduced in a stochastic manner to account for the wires' geometrical irregularities. The mesh model is then validated with reference to a set of punch tests in which the shape and size of the punching element as well as the nominal wire diameter were varied. Subsequently, the model is extended to a punch against soil test configuration permitting an insight into the nontrivial local mechanism between the mesh facing and the underlying granular layer. The good agreement between the numerical predictions and the experimental observations at the laboratory scale allowed us to extend the model towards more realistic field conditions for which the role of the mesh panel boundary conditions, the mesh mechanical properties, the soil mechanical properties and the anchor plate geometry is investigated.

Keywords: Flexible facings; Soil-mesh interaction; Anchor bearing capacity; Wire meshes; Discrete Element Method (DEM)

1. Introduction

Wire mesh systems have largely been used as rockfall mitigation solutions in mountainous regions (Ferraiolo and Giacchetti, 2004; Muhunthan et al., 2005; Volkwein et al., 2011; di Prisco et al., 2010). Only recently have anchored mesh facings been adopted as a stabilizing intervention for shallow granular layers on potentially unstable slopes or in slope cuttings for the realization of infrastructures (Bergado et al., 2000; Bergado and Teerawattanasuk, 2008). This development of their use is due to the high versatility of application combined with a rather rapid installation procedure. Furthermore, they are characterized by a lower environmental and visual impact compared with classic rigid retaining structures (Ferraiolo and Giacchetti, 2004; Muhunthan et al., 2005). A flexible facing is composed of a wire mesh and a pattern of anchor plates (see Fig. 1) connected to tie rods or steel nails, which are grouted in a firm stratum of the slope. The wire mesh can also be combined with a geotextile for erosion prevention and retention of finer materials (Ferraiolo and Giacchetti, 2004; di Prisco et al., 2010).

The effectiveness of an anchored mesh facing in contrasting shallow instabilities in granular slopes is given by the combined action of its components: (i) the wire mesh permits the unstable granular mass to be intercepted and retained, (ii) the anchor plates impose a local contrast to the soil displacement and permits the transfer of the earth-pressure from the mesh to the anchoring system,

* Corresponding author.
E-mail address: antonio.pol@univ-eiffel.fr (A. Pol).

https://doi.org/10.1016/j.sandf.2022.101222

Fig. 1. Example of an anchored mesh facing along a road embankment.

(iii) the nails/ties transmit the stabilizing force to the sliding plane.

The global interaction between a wire mesh system and a granular material has been investigated in previous works (Gabrieli et al., 2018; Pol et al., 2020; Pol and Gabrieli, 2021), where the force–displacement response of the mesh system has been characterized. In this work, it is instead the local behavior at the level of the anchor plates that is addressed.

The characterization of the local contrast imposed by the anchor plates to the soil mass is of fundamental importance in order to move to a proper design of these flexible retaining systems. In fact, it is a key point of a recently proposed design methodology (Galli et al., 2020; Officine Maccaferri S.p.A, 2021), which is based on the concept of a "characteristic" curve that relates the local force acting at the anchored points of the system and the so-called "far-field" displacement of the unstable mass (Galli and di Prisco, 2013; Galli et al., 2017). In the perspective of having an insight into the local interaction mechanism at the anchor plates, a peculiar bearing capacity test configuration, similar to the one adopted in di Prisco et al. (2010), in which a mesh panel is lied above a granular soil layer is considered in this work. A 3D discrete element model is calibrated on experimental data and is used to provide an in-depth analysis of this local mechanism. The experimental tests are described in Section 2, while the numerical methodology and the model calibration is reported in Section 3 and Section 4. A detailed description of the mechanical behavior of the soil-mesh-plate system is given in Section 5. Finally, the main results are summarized in Section 6.

2. Experimental tests

The punch against soil test is an experimental procedure used to estimate the bearing capacity of the soil-mesh-plate system in quasi-static conditions. The experimental setup is composed of a prismatic caisson filled with a dry granular soil. A wire mesh panel with nominal dimension 180 cm×170 cm is lied down on the top of the soil layer and its outer boundary is fixed to a rigid frame. The adopted wire mesh type is a hexagonal double-twisted mesh (referred as DT mesh in what follows) with a nominal wire diameter equal to 3.0 mm. A geotextile is lied between the soil and the mesh panel with the unique role of avoiding the passage of finer particles through the openings of the mesh. It should be noted that the structural role of the geotextile is negligible; in fact its outer border can freely move and the small deformations involved in the problem are not sufficient to activate the tensile response of the geotextile. Finally, the punching device is a flat square anchor plate of 250 mm side commonly adopted in field interventions. The testing procedure consists in moving the punching device downwards, at a fixed displacement rate, against the mesh and the soil layer below. During the test, the force acting on the plate as well as its displacement are registered, providing as test output a force–displacement relation. The test is continued until the failure of the mesh panel is reached (i.e. tearing off the mesh); in all the experimental tests (3 tests were performed) the failure has occurred in the area surrounding the anchor plate. A view of the experimental setup is reported in Fig. 2a, while a detail of the zone surrounding the plate during the test is shown in Fig. 2b.

In order to characterize the mechanical response of the wire mesh, several punch tests on the sole mesh are considered. Experimental data from a UNI standard punch test configuration (UNI 11437, 2012) with a wire mesh of diameter 2.7 mm (T1) were used. Moreover, peculiar punch tests, in which a flat anchor plate is used, with a wire mesh of nominal diameter of 3.0 mm (T2) and 3.9 mm (T3) were considered. The outer boundary of the panel (nominal dimension of 170 cm×160 cm) is fixed to the external frame and a square plate of side equal to 250 mm is used as punching element. The experimental test configurations are summarized in Table 1.

In the mechanical characterization of the mesh, the mesh panel was slightly tensioned before the beginning of each test to minimize the influence of the panel initial conditions linked to the wire geometrical distortion, thus differing from the punch against soil test. The experimental results were provided by Maccaferri Innovation Center (MIC) and will be presented in Section 3.1.1 and Section 4.1.

3. Numerical methodology

3.1. Discrete element modeling of the wire mesh

The discrete element method permits description of a system as an assembly of distinct rigid locally-deformable bodies. Even if the method was originally meant to describe the evolution of granular media, it has been efficiently applied to many geomechanical problems in which discontinuities and interactions between soil particles and struc-

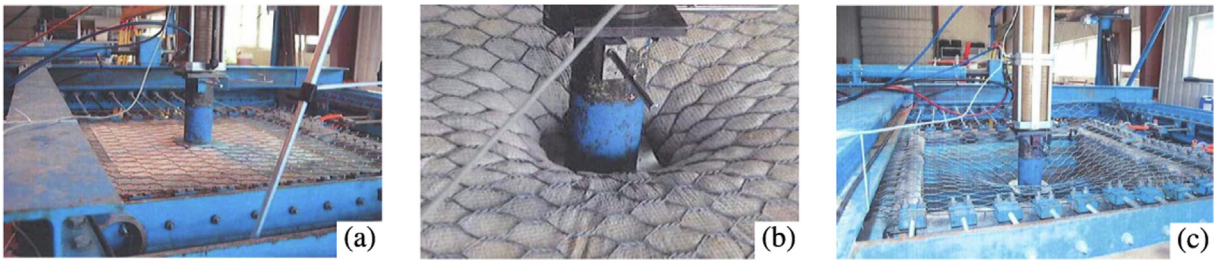

Fig. 2. View of the punch against soil test setup. (a) Overall view and (b) detail of the zone surrounding the plate at an intermediate step of the test. (c) View of the punch test on the sole mesh (courtesy of MIC).

Table 1
Summary of the experimental tests on the sole mesh.

Ref.	Punching element	Mesh type	Wire diam.	# of repetitions
T1	UNI dome-shaped	DT	2.7 mm	5
T2	square-shaped	DT	3.0 mm	6
T3	square-shaped	DT	3.9 mm	4

tural elements are relevant (Calvetti et al., 2004; McDowell et al., 2006; Gabrieli et al., 2009; Ciantia et al., 2016). Recently, the DEM has been applied for investigating the behavior of mesh-like structures (Thoeni et al., 2013; Coulibaly et al., 2017; Gabrieli et al., 2020; Pol et al., 2021a) and to have an insight into their interaction with external bodies (Bertrand et al., 2008; Thoeni et al., 2014; Albaba et al., 2017; Pol and Gabrieli, 2021; Marigo et al., 2021).

In this work, the open source code YADE (Smilauer et al., 2021) is used.

The so-called Node-Wire-Based approach (NWB) (Bertrand et al., 2005; Thoeni et al., 2013; Gabrieli et al., 2017; Pol et al., 2021b) is adopted for the wire mesh numerical description. The NWB approach describes the mesh as a set of spherical particles placed in correspondence to the physical nodes of the real mesh (i.e. intersections between the real mesh wires). The wires are represented by creating long-range interactions between the nodal particles. A graphical scheme of the NWB mesh description is reported in Fig. 3a. It should be noted that the physical shape of the wires is not explicitly discretized, hence the contact with the external body is handled only at the level of the nodal particles (see Fig. 3b). In the numerical model, the diameter of the nodal particles d_n is set equal to four times the nominal diameter of the single wire; this permits a more efficient simulation without modifying the mechanical properties of the mesh (Thoeni et al., 2013; Pol et al., 2021b). The nodal particles' density is modified accordingly in order to maintain the areal density of the real mesh.

The constitutive behavior of the single and double-twisted wires is governed by two different piecewise linear stress–strain relations defined from experimental tensile tests (Thoeni et al., 2013) and shown in Fig. 4. In the DEM model, these relations are used to define the long-range normal contact laws on the basis of the wire diameter and the wire's initial length. Compressive forces as well as bending and torsional stiffnesses of the wire are assumed to play a minor role and are therefore neglected. The breakage of a wire is ruled by a threshold on the maximum elongation (see Fig. 4a), i.e. relative displacement between two nodal particles.

Real mesh panels, especially if not tensioned, are generally characterized by intrinsic geometrical irregularities and distortions of the wire elements. This determines the need of considering the effect of the initial condition of the mesh panel in the numerical model using a stochastically distorted wire model (SDWM) (Thoeni et al., 2013). In the SDWM a stochastical alteration is introduced in the contact laws of the wire elements using the coefficients λ_u

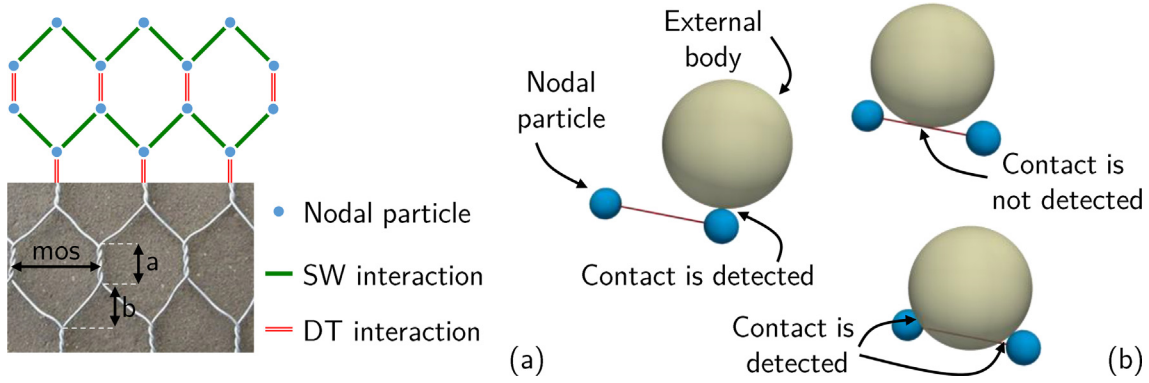

Fig. 3. Numerical model of the wire mesh. (a) NWB description of the wire mesh. (b) Examples of possible contact cases between the mesh nodes and an external body.

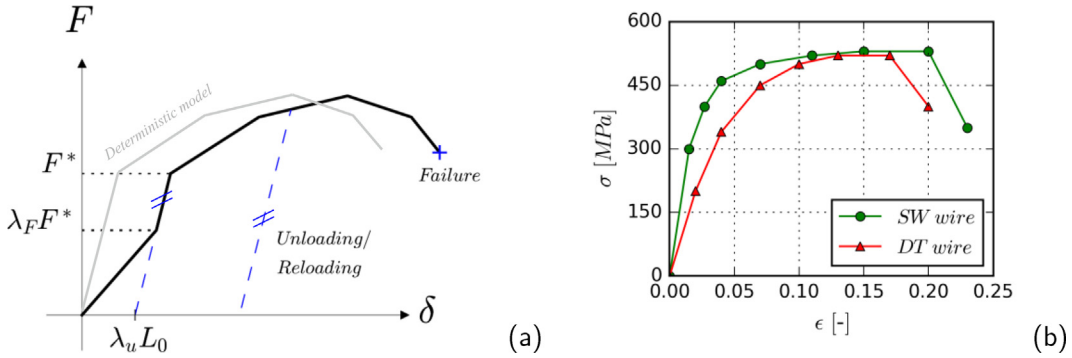

Fig. 4. Mechanical behavior of the mesh wires. (a) Graphical scheme of the stochastically distorted "wire" contact model (SDWM). (b) Experimental tensile stress–strain curves for the single wire (SW) and the double-twisted wire (DT).

and λ_F as shown in Fig. 4a. The coefficient λ_u determines a horizontal shift of the force–displacement curve as a fraction of the initial wire length L_0 (i.e. the initial distance between two interconnected particles); the coefficient λ_F defines instead the reduction of the initial stiffness in the shifted part of the force–displacement curve. The irregularities are randomly distributed on the mesh wires according to a triangular distribution centred in $0.5\lambda_u L_0$. It should be noted that the stochastic parameters λ are not mechanical parameters (i.e. they are not related to the intrinsic mechanical properties of the mesh), but they are linked to the geometrical irregularities of mesh panels when these are not tensioned.

3.1.1. Validation of the mesh model

The experimental punch tests on the sole mesh introduced in Section 2 are used for the mesh model validation. In the experimental procedure, the mesh panel was tensioned before the beginning of the test by slightly moving the punching element, thus recovering the initial distortion of the wires. Therefore, in the numerical model, the stochastic parameter λ_u is set equal to 0 (the value of λ_F is irrelevant for $\lambda_u = 0$, see Fig. 4a), thus using the deterministic force–displacement curves, directly derived from the σ-ϵ curves of Fig. 4b, for the description of the tensile behavior of the wires.

The model is first validated with reference to the results obtained in the UNI standard punch test configuration. The 3 m×3 m mesh panel is described by using 2890 spherical particles. The displacement of the particles belonging to the mesh outer boundary is fixed in order to mimic the constraints imposed in the experimental procedure. The punching element geometry is schematized in the model by using 694 flat triangular elements. A displacement rate of 2 cm/s is imposed on the punching element. The contact parameters adopted in the simulation are reported in Table 2. These are chosen according to previous works (Pol et al., 2021b; Pol and Gabrieli, 2021).

Subsequently, two slightly different experimental configurations (T2 and T3 described in Section 2) are numerically reproduced. In this case the mesh panel has a smaller dimension (1.68 m×1.56 m) and is described by using 862 spherical particles. The punching element geometry has also been varied and is represented by a flat plate of 250 mm side. Moreover, two different wire diameters have been considered (3.0 mm and 3.9 mm). The panel boundary is fixed and the punching element is moved normally with respect to the mesh plane at a constant displacement rate of 2 cm/s. For each test geometry the envelope of the force–displacement curve obtained in the test repetitions is displayed in Fig. 5. The numerical results are in good agreement with experimental data and correctly account for effects related to the punching element shape and size, the mesh panel dimension, and the nominal diameter of the mesh wires.

Table 2
Contact parameters of the mesh model.

Micromechanical elastic modulus, E_s [Pa]	20×10^9
Tangent to normal contact stiffness coefficient, ν_s [-]	0.30
Contact friction angle, ϕ_s [°]	35.0

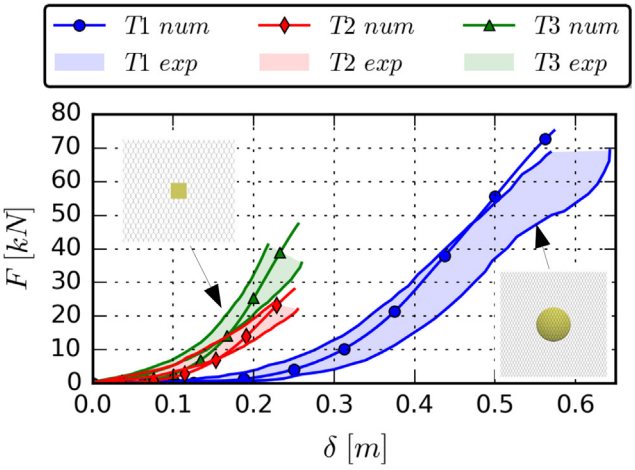

Fig. 5. Comparison between numerical and experimental punch test results. Test T1 refers to a UNI standard punch test configuration, while test T2 and test T3 refer to the anchor punch test on the sole mesh for a nominal diameter of the mesh of 3 mm and 3.9 mm respectively. For each of test configuration, the envelope of experimental repetitions is displayed.

3.2. Modeling of the granular layer

The granular volume is simulated by using spherical particles whose mean diameter is set equal to 40 mm (polydispersity of 5% to avoid crystallization). This corresponds to the diameter of the coarse fraction of the material adopted in the experimental tests. The choice of using a slightly up-scaled modeling approach was dictated by: (i) a sake of computational efficiency, (ii) to avoid the passage of the particles through the mesh openings. This modeling approach has been used in several works (Calvetti et al., 2004; Calvetti and Nova, 2004; Gabrieli et al., 2009) and, once the numerical parameters are properly calibrated, it permits realistic reproduction of the global behavior of the system.

The contact model adopted for the description of the interaction between soil particles is the standard linear force–displacement model for the normal contact and linear with a frictional plastic limit for the tangential contact (Cundall and Strack, 1979). The normal and tangential contact forces are given by:

$$F_n = k_n \delta \tag{1}$$

$$\Delta F_t = k_t \dot{u}_t \mathrm{d}t \quad (|F_t| \leqslant |F_n| \tan \phi_s) \tag{2}$$

where k_n and k_t are the normal and tangential contact stiffness respectively, δ is the interpenetration at the contact, ϕ_s the contact friction angle, $\dot{u}_t$ is the relative tangential velocity between the two bodies and dt is the time step of the integration scheme. The contact normal stiffness is given by (Smilauer et al., 2021):

$$k_n = 2\frac{E_{s,i}R_i E_{s,j}R_j}{E_{s,i}R_i + E_{s,j}R_j} \tag{3}$$

where E_s is the micromechanical elastic modulus and R is the particle's radius; in Eq. 3 subscripts i and j represent the i-th and j-th particles in contact. The tangential contact stiffness is linearly related to the normal one through the coefficient v_s ($k_t = v_s k_n$).

To account for the nonspherical shape of the particles composing the real granular material, a rolling resistance is introduced at the particles' contact. This permits the shape effect to be accounted for without drawbacks in terms of computational efficiency (Iwashita and Oda, 1998; Belheine et al., 2009; Wensrich and Katterfeld, 2012). In YADE, the rotational law at the contact is ruled by two dimensionless parameters: the rotational stiffness coefficient β_r and the rotational resistance coefficient η_r. The rolling stiffness is defined as in Eq. 4, while the plastic limit is given by Eq. 5.

$$k_r = \beta_r R_i R_j k_t \tag{4}$$

$$M_r \leqslant \eta_r F_n \min\left(R_i, R_j\right) \tag{5}$$

4. Numerical model of the punch against soil test

The granular soil underlying the mesh panel is represented by a prismatic volume (1.76×1.64×1.00 m^3) composed of approximately 47000 spherical particles with a mean diameter of 4 cm and a density ρ_s equal to 2500 kg/m^3. The soil mass is laterally contained by four walls and a bottom layer of particles is fixed to simulate the basal support. The mesh panel of dimension 1.76 m×1.64 m (the same dimension of one of the three experimental tests) is discretized by using 946 spherical particles. According to the experimental procedure, the panel's outer boundary is fixed by imposing a no-displacement condition on the nodal particles belonging to the mesh panel edges. Furthermore, a square anchor plate of side $b = 250$ mm is used as the punching element.

In the experimental punch against soil test, due to the presence of the soil layer, the mesh panel was not tensioned prior to the test and therefore the wires were initially distorted. This determines the need to account for the initial geometrical configuration of the mesh in the numerical model by introducing a stochastic distortion of the force–displacement curves of the wires. The calibration of the mesh's stochastic contact parameters λ_u and λ_F will be discussed in Section 4.1. A 3D view of the numerical model is reported in Fig. 6.

In a preliminary phase, the granular volume is let settle under gravity until obtaining a stable sample. Then, the top layer is regularized to obtain an almost planar surface, the mesh panel is created in adherence to it and the mesh is let settle over the soil particles under gravity. After this phase, a constant displacement rate of 2 cm/s is imposed on the plate, thus ensuring quasi-static conditions. It should be noted that negligible differences in the mechanical response of the system were observed for lower displacement velocities of the anchor plate, confirming the absence of inertial effects. The test is ended after the complete failure of the mesh that corresponds to the rupture of the wires intercepted by the anchor plate.

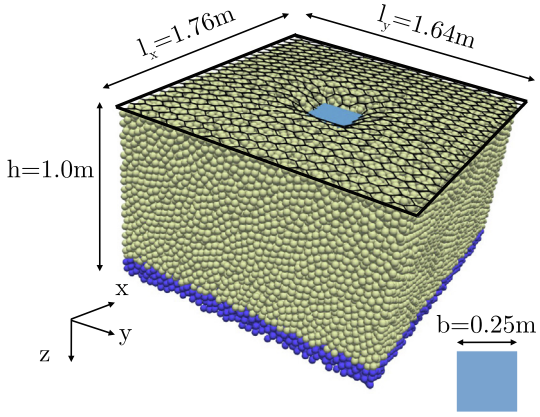

Fig. 6. 3D view of the numerical model of the punch against soil test: the black thick line represents the fixed boundary of the mesh, the fixed soil layer is highlighted in blue.

4.1. Calibration of the numerical model

The contact parameters of the soil particles and of the SDWM parameters are calibrated with reference to the experimental results of the punch against soil test according to a two-phase procedure as described in what follows.

For low displacements of the anchor plate (i.e. $\delta \leqslant$ 35 mm in this case, see Fig. 7), the system's response is controlled by the soil reaction only, while the contribution of the mesh is negligible. The soil contact parameters are therefore calibrated referring to the first part of the experimental force–displacement curve. It has been shown that the contact parameters can be calibrated separately (Calvetti et al., 2003; Sibille et al., 2007; Belheine et al., 2009). Therefore, following standard DEM calibration practice, elastic parameters are tuned at first since they control the stiffness of the system, then the contact strength parameters are considered (Plassiard et al., 2009; Gabrieli et al., 2009; Cheng et al., 2018) to match the peak and post-peak material strength.

For further increments of the anchor plate displacement, a strong variation of the trend of the F-δ curve is observed. This is related to the onset of a first failure mechanism in the soil layer due to the overcoming of the soil bearing capacity that, for the soil and for the anchor plate here considered, is observed for a punching force of approximately 85 kN. This induces a lateral spreading of the soil, which starts to interact with the mesh. From this moment, the mesh mechanical response is progressively activated, partially by the soil upwards and lateral movement outside the plate footprint, and partially by the anchor plate displacement. The mechanical response of the system is significantly influenced by the mesh reaction from now on, hence the final part of the F-δ curve, i.e. $\delta \geqslant$ 35 mm, is used as a reference to calibrate the stochastic parameters associated with the mesh numerical model (i.e. λ parameters of the SDWM). A graphical representation of the effect of the contact parameters on the system response observed in the calibration phase is reported in Fig. 7. The calibrated contact parameters are reported in Table 3.

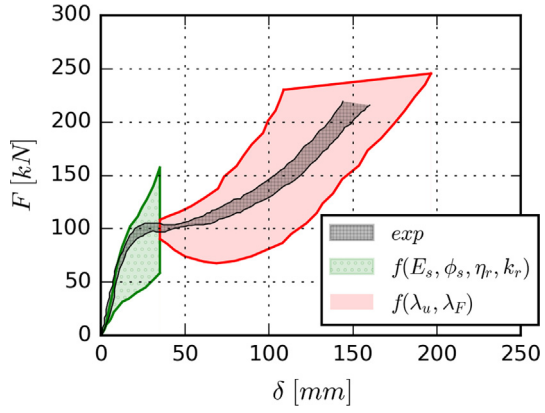

Fig. 7. Graphical representation of the effect of the contact parameters on the system's mechanical response: green dotted (soil parameters) and red (mesh parameters) areas represent the envelopes of the numerical trial curves when changing the parameters in brackets. The dark gray hatched area represents the envelope of the experimental results.

The obtained force–displacement response well reproduces the mechanical behavior observed in the experimental test from low displacements (soil response) to the failure of the mesh as shown in Fig. 8a. Furthermore, the failure modality observed in the numerical model (see Fig. 8b) is coherent with what was observed in the experimental campaign: some local ruptures of the wires in correspondence to the anchor plate boundary were initially observed, then nearby wires fail in rapid succession.

5. Mechanical behavior of the system

In this section, the local interaction mechanism between the mesh, the anchor plate and the soil layer is discussed. In this perspective, the contribution of the system's components is separately considered by using the following definitions (see also Fig. 9):

- the overall force sustained by the system F_{SM}, given by the total force acting on the anchor plate;
- the force sustained by the mesh F_M, given by the sum of the tensile forces acting on the wires converging on the edges of anchor plate;
- the force sustained by the mesh without the presence of the soil layer F^*_M, which is derived from a further simulation in which the soil layer was not considered. Same stochastic parameters of the test against the soil were used ($\lambda_u = 0.05$, $\lambda_F = 1$);
- the force sustained by the soil without the presence of the mesh F^*_S, which is derived from a further simulation in which the mesh was not considered.

In Fig. 9b the force–displacement curve of the overall system (SM) is compared with the one obtained from a punch test against the solely soil layer (S^*). It can be observed that the two curves are almost identical for low displacements, thus showing that the mechanical response in the first part of the test is controlled uniquely by the soil reaction. Regarding the force–displacement response of the system at large-displacement values, when comparing curve S^* and curve SM, one can acknowledge that the insertion of the wire mesh causes a significant increase of the force with the plate's displacement. From a quantitative perspective, the system bearing capacity (i.e. the maximum force registered during the test) goes from 84.8 kN for the case

Table 3
Calibrated numerical parameters.

	E_i [Pa]	ν_i [-]	ϕ_i [°]	β_r [-]	η_r [-]	λ_u [-]	λ_F [-]
mesh	20×10^9	0.30	35.0	-	-	0.05	1.00
soil	1×10^9	0.30	47.5	0.02	0.06	-	-
plate	1×10^9	0.30	35.0	-	-	-	-
box	1×10^9	0.30	0.0	-	-	-	-

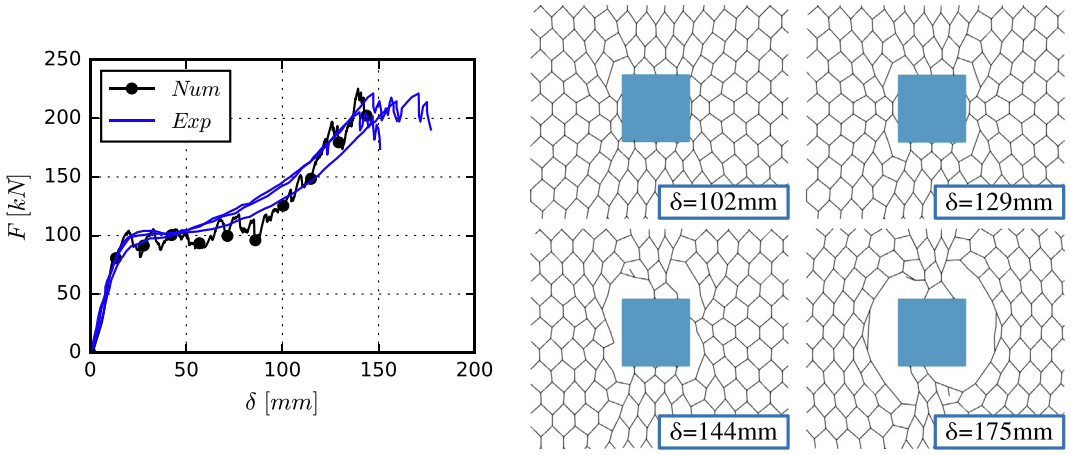

Fig. 8. Mechanical response of the punch against soil test. (a) Comparison between numerical and experimental results. (b) Mesh failure modality observed in the punch against soil test numerical model.

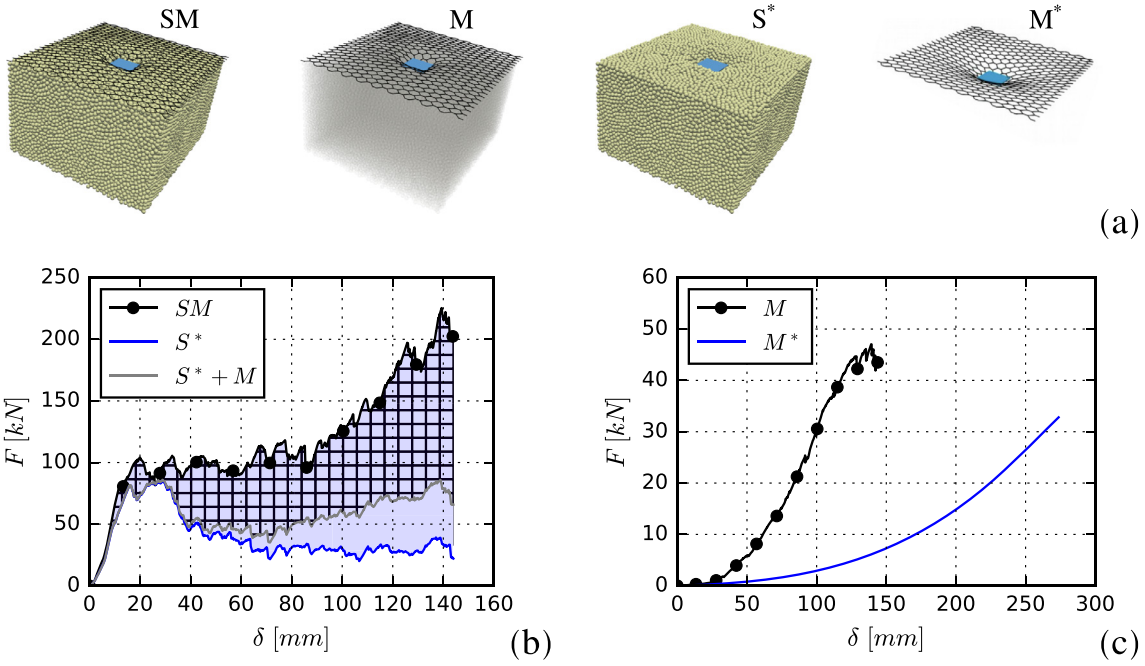

Fig. 9. Contribution of the system's components to the overall response. (a) Graphical explanation of the force associated to the system's components. (b) Mechanical response of the system with (SM) and without (S^*) the presence of the mesh. (c) Comparison of the mesh mechanical response with (M) and without (M^*) the presence of the soil layer.

S^* to 225.4 kN for the case SM, thus obtaining a bearing capacity ratio $BCR = 2.66$. Moreover, the presence of the wire mesh permits larger displacements of the plate to be reached before the failure of the system.

The benefit provided by the introduction of the mesh on the mechanical response of the system is highlighted in Fig. 9b (blue area). It should be noted that the enhancement in the system resistance is only partially due to the mesh mechanical resistance; a large contribution is, in fact, provided by the interaction between the granular soil and the wire mesh. This aspect can be better understood by referring to the curve $S^* + M$ reported in Fig. 9b, which describes the mechanical contribution provided by the soil and by the mesh, if taken separately. The contribution associated to the soil-mesh interaction can therefore be estimated as the difference between the curves SM and $S^* + M$; this is graphically represented by the gray hatched area in Fig. 9b. The fundamental role of the soil-mesh interaction is evident when considering the maximum force registered in the SM case: the contribution provided by the solely mesh (M) is $\approx$ 47 kN, while the one associated with the soil-mesh interaction is $\approx$140 kN ($\approx$ 62% of the bearing capacity of the system).

The action exerted by the mesh is negligible in the first part of the test, then it increases when the soil starts to spread laterally to the anchor plate. From the soil perspec-

tive, the wire mesh applies a frustration to the lateral and upwards bulging mechanism, thus leading to a progressive enlargement of the "effective footprint" of the plate. It should be noted that, since the particles cannot pass through the mesh openings, the mesh acts as a flexible membrane on the soil layer (Li and Zhao, 2018; Pol and Gabrieli, 2021). On the other hand, the presence of the soil, represents a "soft constraint" for the mesh "free" displacement along the z-direction. This effect is particularly significant in the area surrounding the anchor plate where the mobilized soil volume applies an upward thrust against the mesh. The contrast imposed by the soil to the mesh displacement determines a prompter reaction of the mesh panel with respect to what was observed performing a test on solely mesh (case M^*); moreover, the mesh shows a higher punching resistance when interacting with a granular layer as can be observed in Fig. 9c. The constraint imposed by the soil layer to the mesh z-displacement and the emergence of the uplift mechanism in the zone surrounding the anchor plate are particularly evident when observing the deformed configurations in the xz-plane of the central section of the mesh, with and without the presence of the soil, as reported in Fig. 10. A similar deformed profile was observed with reference to the yz-plane.

5.1. Force transmission mechanism

In Section 5 the mechanical behavior of the system has been analyzed from a macroscopic perspective, namely, considering the overall force–displacement response of the system. The particle-based approach adopted in this work permits one to access micromechanical information, as, for instance, the contact forces exchanged between the soil particles or between the soil particles and the nodal particles of the mesh.

It is well known that, when a granular material is subjected to an external load, its particles tend to rearrange themselves into oriented structures to contrast the applied load (Andreotti et al., 2013). Considering only the contact forces larger than the mean contact force (i.e. strong force network), it is notable that the orientation of these forces is not arbitrary, but follows the direction of principal stresses. In order to highlight the evolution of these forces in the soil layer, a x-oriented and a y-oriented slices of thickness equal to the anchor plate side ($b = 25$ cm) of the soil domain are used as reference volumes (see Fig. 11). Then, the force network is condensed in a 2D view as reported in the plots of Fig. 11. The plate displacement determines the formation of a root-shaped network of contact forces that develops in a truncated conical volume of the soil layer; it is notable that, during the test, this volume not only deepens along the z-direction but also becomes wider in both the x-direction and y-direction as shown in Fig. 11. The mobilized soil volume progressively increases with the plate displacement, and it provides an active contrast to the plate during the entire test. This possibility is granted by the presence of the wire mesh that limits the lateral spreading of the soil around the plate. The comparison of the force network observed with reference to the xz-plane and the yz-plane shows that the pressure cone in the soil layer is wider along the y-direction. This can be reasonably related to anisotropic response of the hexagonal double-twisted wire mesh along its two principal directions (Pol, 2020; Pol et al., 2021b).

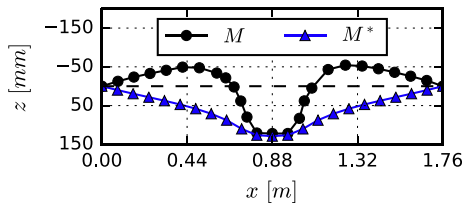

Fig. 10. Deformed mesh profile in the xz-plane, with (M) and without (M^*) the soil layer, with reference to the central section at $\delta = 140$ mm.

To have a better understanding of the confinement imposed by the mesh on the soil layer, the forces exchanged at the contact between the mesh nodes and the soil particles are considered. The confining pressure p_{ms} is hence computed by subdividing the mesh surface in a regular grid with a spacing of 4 cm (i.e. minimum spacing between the nodes of the mesh) and by dividing the sum of the normal force (with respect to the mesh-soil contact) pertaining to each grid cell by the cell's area. The portion of the mesh under the anchor plate is neglected in this analysis since it is not directly imposing a confining pressure on the soil layer. Following the same procedure, but now considering the tangential forces, the tangential confining pressure τ_{pm} is computed. The top view of the confining pressure distributions on the entire panel surface are reported in Fig. 12 with reference to a plate displacement level of 140 mm. The pressure p_{ms} concentrates in the area surrounding the anchor plate and strongly reduces when moving far from it. A larger confining pressure p_{ms} is observed along the y-direction (double-twisted wire orientation) than along the x-direction as a consequence of the anisotropic mechanical behavior of the mesh. An analogous distribution is also observed when considering the tangential pressure at the mesh-soil contact τ_{ms}.

The evolution of the confining pressure distribution along two slices of thickness 25 cm (yellow areas in the inset of Fig. 13) is considered. The pressure value is computed as the mean of the grid cell pressure values on a strip of 4 cm×25 cm (small red areas in the inset of Fig. 13). The time evolution of pressure p_{ms} is shown in Fig. 13a and Fig. 13b with reference to a x-oriented and a y-oriented slice respectively. In both directions, the confining pressure increases with the plate displacement. Furthermore, the trend of p_{ms} shows that the confining action exerted by the mesh on the soil enlarges up to a distance of approximately $1.3b$ from the plate's edge, once the mesh reaction is mobilized. The anisotropic mechanical behavior of the mesh is evident when comparing the magnitude of the con-

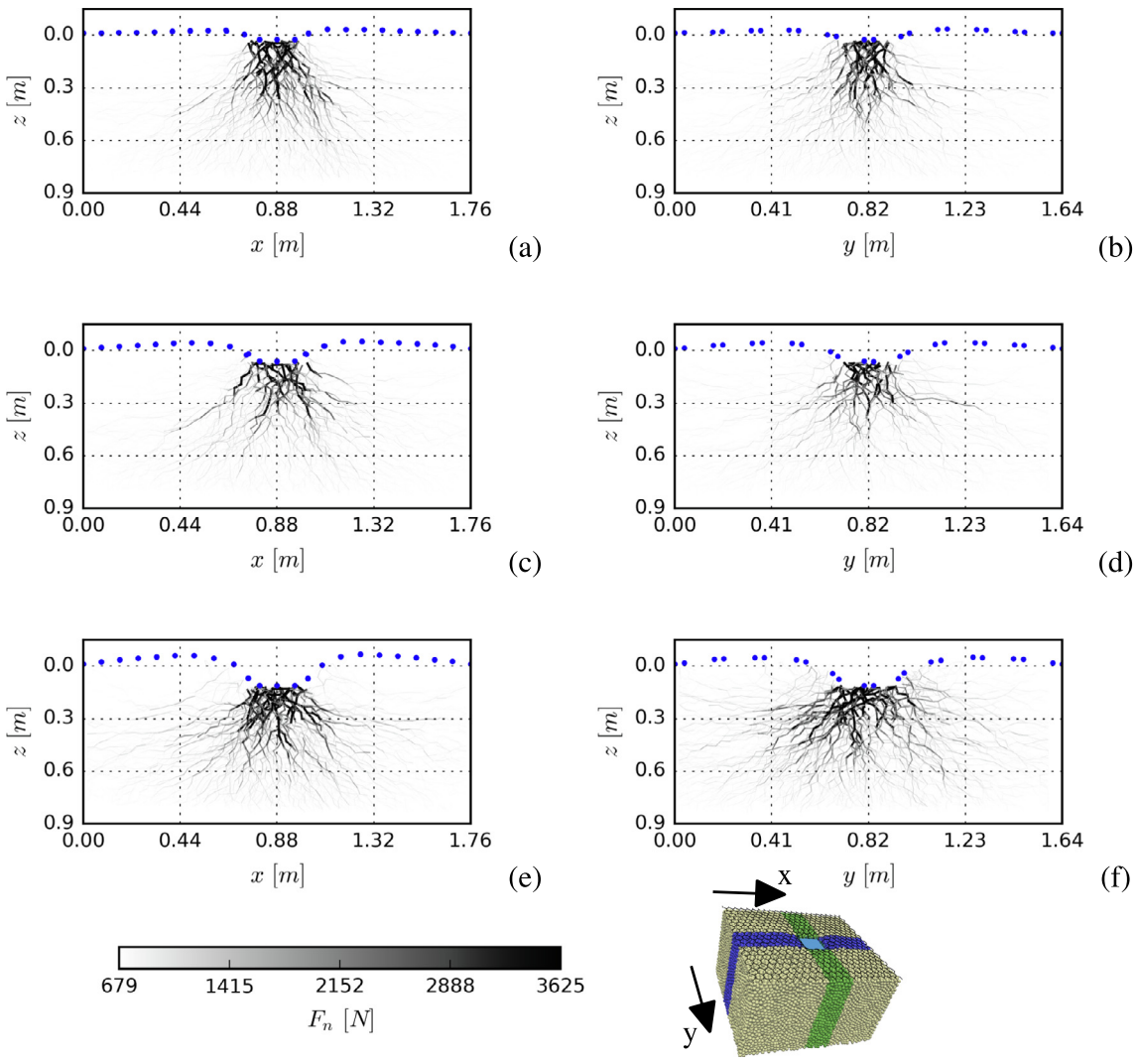

Fig. 11. Contact force network at different displacement levels of the anchor plate: $\delta = 20$ mm (a) xz-plane and (b) yz-plane, $\delta = 65$ mm (c) xz-plane and (d) yz-plane, $\delta = 140$ mm (e) xz-plane and (f) yz-plane (the colorbar upper limit is set to $\max(F_n)/4$ for the sake of readability). The slices of the soil domain considered in the analysis are highlighted in blue and green.

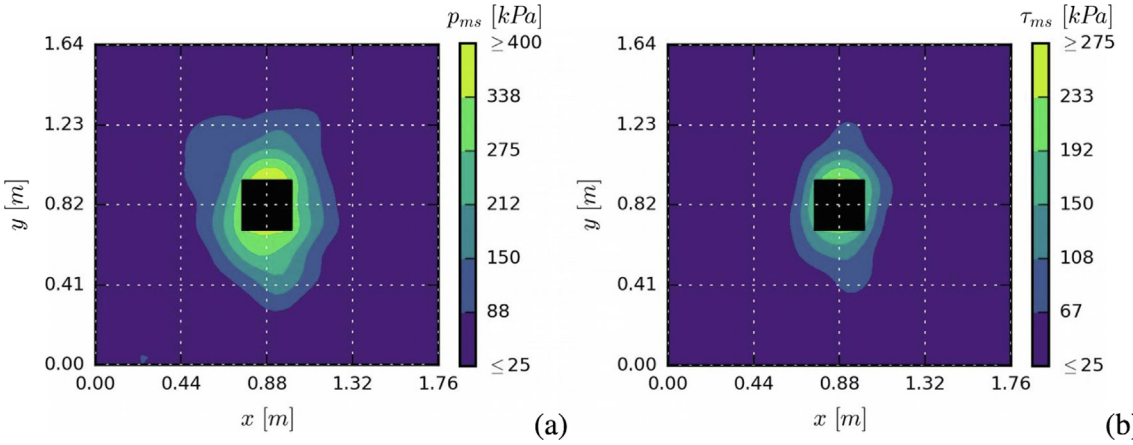

Fig. 12. Confining pressure distributions. (a) Normal confining pressure p_{ms} and (b) tangential confining pressure τ_{ms} at the mesh-soil interface for a displacement level of the anchor plate $\delta = 140$ mm.

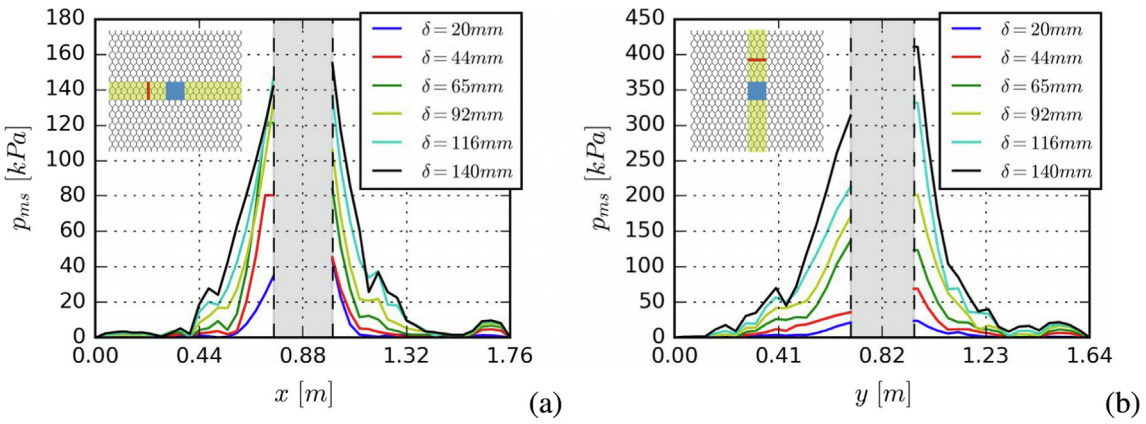

Fig. 13. Normal confining pressure p_{ms} distribution along (a) the x-direction and (b) the y-direction. The pressure is computed as the mean of the grid cell pressure values on a strip of 4 cm×25 cm (small red area in the inset). The yellow area in the inset represents the portion of the mesh considered in the plots.

fining action exerted by the mesh along its two principal directions. The pressure exerted along the y-direction (i.e. double-twisted wire orientation) is almost twice bigger than the one observed along the x-direction. This determines a higher soil confinement along the y-direction and may explain the larger extension of the strong force network observed in such direction.

5.2. Soil displacement field

The evolution of the displacement field in the soil layer is here addressed. Two slices of thickness 25 cm are considered as done in Section 5.1. Similar results were obtained with reference to the xz-plane and the yz-plane, therefore only the results related to the former are reported in what follows. The slice is divided in a bi-dimensional regular xz-grid. A displacement value is associated to each grid cell by computing the mean displacement of all particles whose center is contained in the considered grid cell. The time evolution of the z-displacement field is reported in Fig. 14. It should be noted that the soil volume is reported only up to 50 cm depth since negligible displacements were observed for deeper layers.

The evolution of the displacement field observed in the numerical model is very similar to the one typical of a shallow foundation problem: a soil wedge under the plate, that is rigidly following the plate movement (red zone in Fig. 14), and two lateral volumes that are bulging and sliding upwards (blue zones in Fig. 14). This result is not surprising considering that the punch against soil test can be seen as a "special" bearing plate test. In this perspective, the mesh effect may be considered as an increment of the "effective footprint" of the plate, which contrasts the lateral spreading of the soil in the area surrounding the plate.

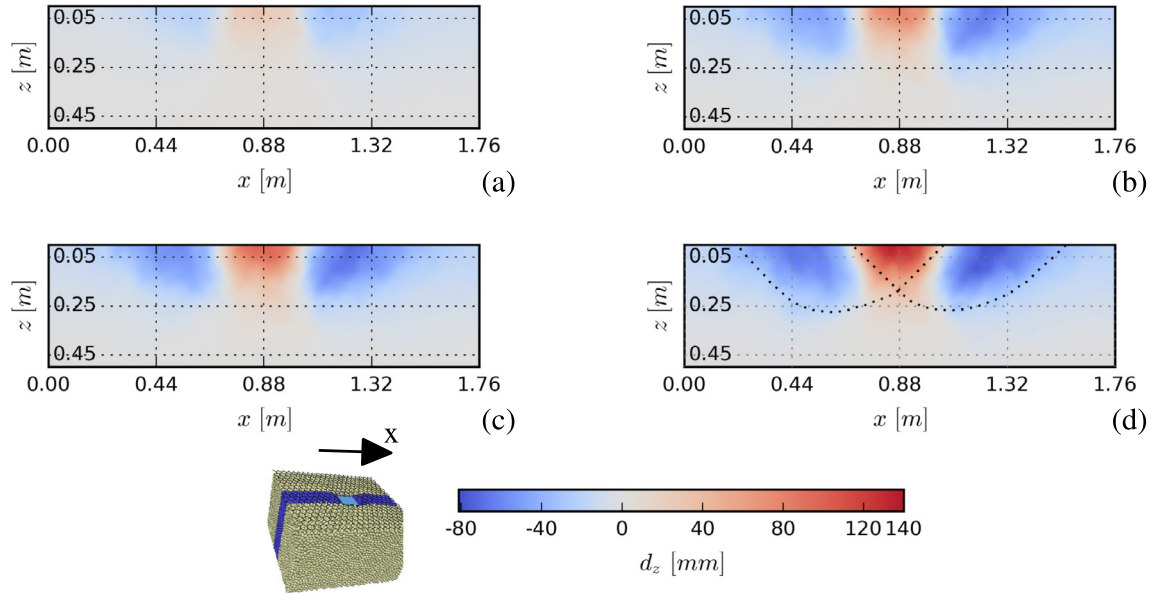

Fig. 14. Time evolution of the z-displacement field in the soil layer: (a) $\delta = 20$ mm, (b) $\delta = 65$ mm, (c) $\delta = 92$ mm, (d) $\delta = 140$ mm. The slice of the soil domain considered in the analysis is highlighted in blue.

When comparing the displacement field obtained with and without the presence of the mesh (see Fig. 15), it can be noted that in the former case the soil emergence zones move laterally with respect to the anchor plate edges; this is in agreement with what has been observed in Boschi et al. (2021). Moreover, the confining action exerted by the mesh determines a deepening of the failure surface and a consequent general increase of the soil volume involved in the bulging mechanism.

In light of the results on the contact force network and the confining pressure distribution the mechanical response of the system can be subdivided in three "steps":

- for $\delta \leqslant 20$ mm, the mesh reaction to the plate displacement is negligible as well as the confining pressure that the mesh imposes on the soil volume (see p_{ms} distribution for $\delta = 20$ mm in Fig. 13). In this first step of the test, the behavior of the system is controlled uniquely by the mechanical response of the soil layer;
- for 20 mm $< \delta \leqslant 65$ mm, the mesh starts to recover the initial deformation and is progressively tensioned. The contribution of the mesh in contrasting the plate displacement is still negligible. Nevertheless, the mesh starts to exert a confining pressure on the underlying granular layer (see p_{ms} distribution in Fig. 13) that permits the lateral spreading of the soil to be controlled, thus avoiding the full development of a failure mechanism in the soil layer;
- for $\delta > 65$ mm, the contribution of the mesh in contrasting the plate displacement is progressively activated until the failure of the mesh. The confining pressure exerted by the mesh on the soil layer progressively increases during this entire step (see p_{ms} distribution in Fig. 13), thus permitting a larger soil volume to actively contrast the plate displacement.

A schematic representation of the failure mechanism observed with and without the presence of the mesh is reported in Fig. 16. The confining action that the mesh exerts on the soil layer determines a deepening of the failure surface and a lateral shift of the emerging zone with respect to the plate edges. The contact force networks in

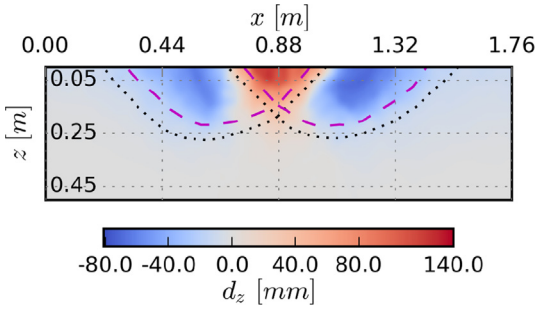

Fig. 15. z-Displacement field obtained without the presence of the mesh with reference to a plate displacement δ of 140 mm. The black dotted line represents the failure mechanism observed with the presence of the mesh.

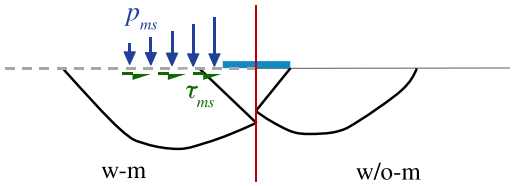

Fig. 16. Comparison of the failure modes observed with (w-m) and without (w/o-m) the mesh.

the granular layer, obtained with and without the mesh, are compared in Fig. 17. Initially, the force network is similar in both cases, confirming the negligible influence of the mesh for low displacements. For larger displacements of the plate, instead, a significant difference in the force network is observable. The confining action exerted by the mesh permits a larger soil volume to be mobilized, as highlighted by the wider and deeper force network in Fig. 17b-c. This retards the onset of the failure mechanism in the granular layer and results in an enhanced contribution of the soil to the bearing capacity of the system.

5.3. Towards an in situ condition: effect of the boundary conditions

The test configuration considered up to this point faithfully represented the laboratory testing conditions (i.e. fixed outer boundary of the mesh panel). This has permitted the calibration of the numerical parameters (Section 4.1); moreover, the mechanical analysis conducted in Section 5 has given an insight into the interaction mechanism of the soil-mesh-plate system. Nevertheless, the boundary conditions imposed on the mesh panel in the laboratory test are not representative of field applications, in which the mesh is only locally constrained by the presence of a pattern of anchor plates. To move towards a more realistic description of the field conditions symmetric boundary conditions are used (see Fig. 18). This choice permits one to consider a realistic constraint of the mesh and at the same time to account for the effect of adjacent panels (Pol et al., 2021b; Pol and Gabrieli, 2021). This test configuration will be referred as "in situ" punch against soil test in what follows.

The numerical results are reported in Fig. 19 where they are compared with the ones related to the laboratory test configuration and the mechanical response obtained when considering the solely soil layer. From a qualitative point of view, the overall mechanical behavior of the system is analogous to the one observed in the standard laboratory conditions. The mesh panel, even if not fixed along its outer boundary, exerts a confining pressure on the soil layer, thus permitting an enhancement of the bearing capacity of the soil-mesh-plate system with respect to the one observed when considering the soil layer only (see Fig. 19a). The maximum force registered during the test increases from 84.8 kN to 147 kN with the presence of the mesh ($BCR = 1.73$).

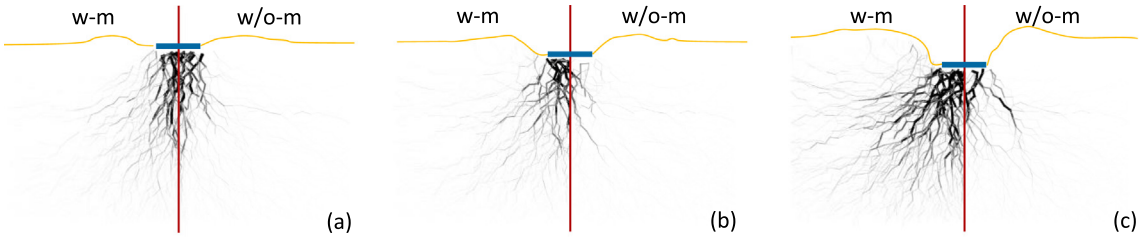

Fig. 17. Comparison of the contact force networks (yz-plane) observed with (w-m) and without (w/o-m) the mesh at different displacement level: (a) $\delta = 20$ mm, (b) $\delta = 65$ mm, (c) $\delta = 140$ mm. The yellow line indicates the soil profile.

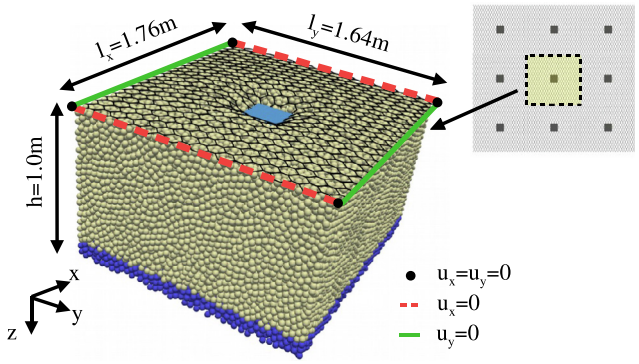

Fig. 18. 3D view of the numerical model of the "in situ" punch against soil test.

The main effect related to the modification of the mesh boundary conditions is observable in the drop of the F-δ curve in the intermediate phase of the test, i.e. 30 mm $\leqslant \delta \leqslant$ 90 mm. This can be related to a lower confining pressure exerted by the mesh in this phase of the test, which is due to a retarded reaction of the mesh dictated by the "softer" boundary conditions. In the final part of the test, the effect of the mesh panel boundary conditions is almost negligible and a similar increasing trend of the force–displacement curve is observed in the two configurations. Furthermore, the pure mechanical contribution of the mesh is only slightly affected by the boundary conditions as notable in Fig. 19b. The difference in the bearing capacity is therefore imputable to the temporary reduction of the system's reaction to the plate displacement in the intermediate phase of the test.

In the analyses reported above, the mechanical characteristics of the mesh, of the granular layer and of the anchor plate dimension were kept constant. Hereafter, the main results of a parametric analysis are reported with the aim of understanding the role of the problem's variables on the system mechanical behavior. The "in situ" test configuration will be used as the reference one in what follows.

5.3.1. Effect of the mesh mechanical properties

The mechanical properties of the mesh are modified considering a different nominal diameter of the wires, but keeping constant the stress–strain curve and the contact parameters. This allows the strength and stiffness of the mesh to be modified, without changing the mesh typology. Three commercial nominal wire diameters are used, namely, $d_w = 2.0$ mm, 3.0 mm, 3.9 mm.

The overall mechanical response of the system obtained by considering different values of d_w is reported in Fig. 20a. As expected, the bearing capacity of the system increases when using a larger wire diameter; this moves from 102.6 kN for $d_w = 2.0$ mm to 243.7 kN for $d_w = 3.9$ mm. Consequently, an increase of the nominal wire diameter results in a significant increase of the bearing capacity ratio: $BCR = 1.21$ for $d_w = 2.0$ mm, $BCR = 1.73$ for $d_w = 3.0$ mm, $BCR = 2.87$ for $d_w = 3.9$ mm. However, only a minor part of the observed increment in the bearing capacity is

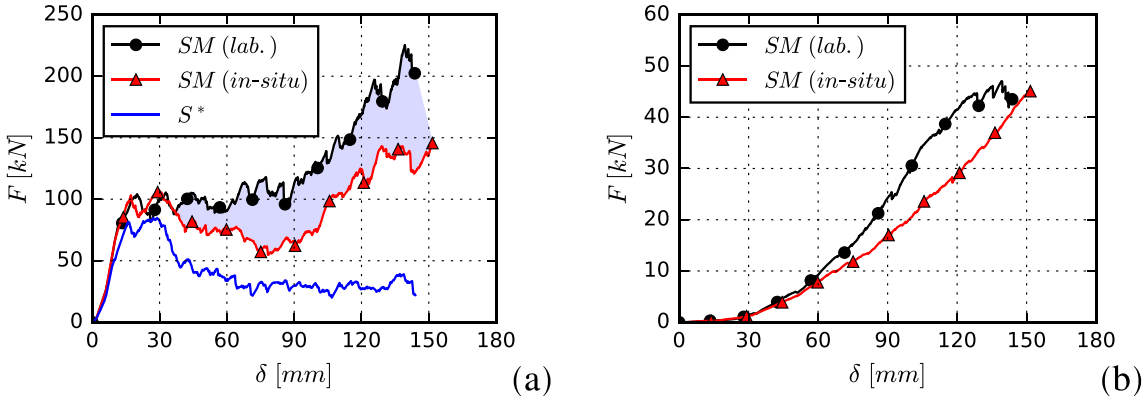

Fig. 19. Comparison of the mesh mechanical behavior obtained by using the laboratory and "in situ" boundary conditions: (a) overall system response and (b) mesh response.

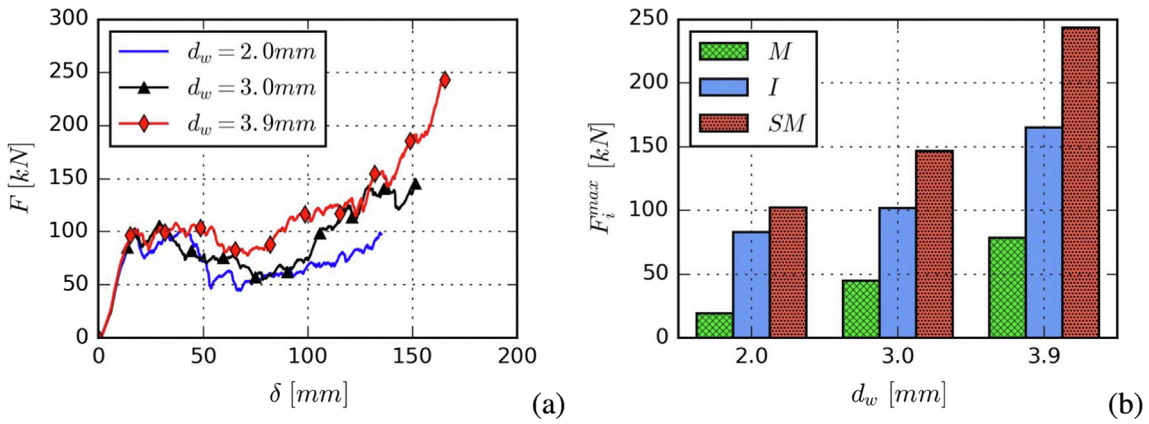

Fig. 20. Effect of the mesh mechanical properties. (a) Comparison of the system's mechanical behavior obtained by considering a different nominal diameter of the mesh wires. (b) Force values at failure for the overall system (SM) and partial contribution provided by the mesh (M) and by the mesh-soil interaction (I).

due to the higher puncturing resistance of the mesh, while the main contribution is related to an improved interaction between the mesh and the soil layer. It is interesting to note that the temporary loss in the system resistance in the intermediate part of the test is lower when using a stiffer mesh. Following this trend, it can be inferred that for wire meshes characterized by a high-tensile stiffness, the plateau observed at intermediate displacements could disappear: in that case the mesh would behave as a semirigid extension of the anchor plate footprint. A stiffer mesh can, in fact, exert a higher normal pressure on the soil surface for the same amount of the plate displacement; this determines a higher contrast to the lateral spreading of the soil and may permit the upward sliding of the lateral soil volumes to be significantly retarded.

To quantify the benefit in terms of mesh-soil interaction, related to the adoption of a higher wire diameter, the contribution to the system bearing capacity derived from the mesh-soil interaction (I) is computed by subtracting from the maximum force registered during the test (i) the punching resistance of the mesh (M) and (ii) the contribution of the soil (S^*), which is $\approx$ 38kN independently of d_w; the soil contribution is estimated from the case S^* (see Fig. 9b) as the mean value in the post-peak portion of the curve (i.e. $\delta \geqslant 60$ mm). The obtained values are reported in Fig. 20b where the increment of the force contribution related to the mesh-soil interaction as well as the increase of punching resistance of the mesh with the wire diameter can be noted.

5.3.2. Effect of the soil type

In order to modify the soil type, different sets of contact rolling parameters are considered. This mainly acts on the macroscopic soil strength and particularly on the emergence of a peak frictional behavior (Belheine et al., 2009). The adopted sets of numerical parameters are reported in Table 4.

A mechanical characterization of the macroscopic behavior of the different soil types was obtained from 3D numerical drained triaxial tests conducted on periodic samples following the procedure described in Pol and Gabrieli (2021). For each set of numerical parameters, four triaxial tests at different confinement pressures (50 kPa, 75 kPa, 150 kPa and 225 kPa) have been performed. The same porosity that characterizes the soil volume in the punch against soil test (i.e. $n = 0.385$) is reached before the beginning of the deviatoric phase for all tests. The obtained macroscopic elastic modulus E_{50}^M and peak friction angle ϕ_s^M are reported in Table 5.

Table 4
Numerical contact parameters of the different soil types.

Type	E_s [Pa]	ϕ_s [°]	β_r [-]	η_r [-]
1	1×10^9	47.5	0.000	0.00
2	1×10^9	47.5	0.005	0.01
3	1×10^9	47.5	0.010	0.03
ref	1×10^9	47.5	0.020	0.06

The mechanical response of the system observed when considering the different soil types is reported in Fig. 21a. A higher bearing capacity of the system is obtained when increasing the macroscopic soil friction angle, as expected. This increment is mostly related to the increase of the soil bearing capacity (reaction for low displacements). The contribution provided by the mechanical resistance of the mesh is instead approximately the same in all considered cases; only a slight difference in the stiffness of the mesh response is observed, which may derive from the "softer"

Table 5
Macroscopic parameters obtained from numerical triaxial tests for the different soil types (the value in round brackets gives the range of variation observed by varying the confining pressure).

Type	E_{50}^M [MPa]	ϕ_s^M [°]
1	218 (±8.5)	28.0 (±1.0)
2	220 (±6.5)	31.5 (±1.0)
3	209 (±5.0)	35.5 (±0.5)
ref	204 (±5.0)	40.0 (±0.5)

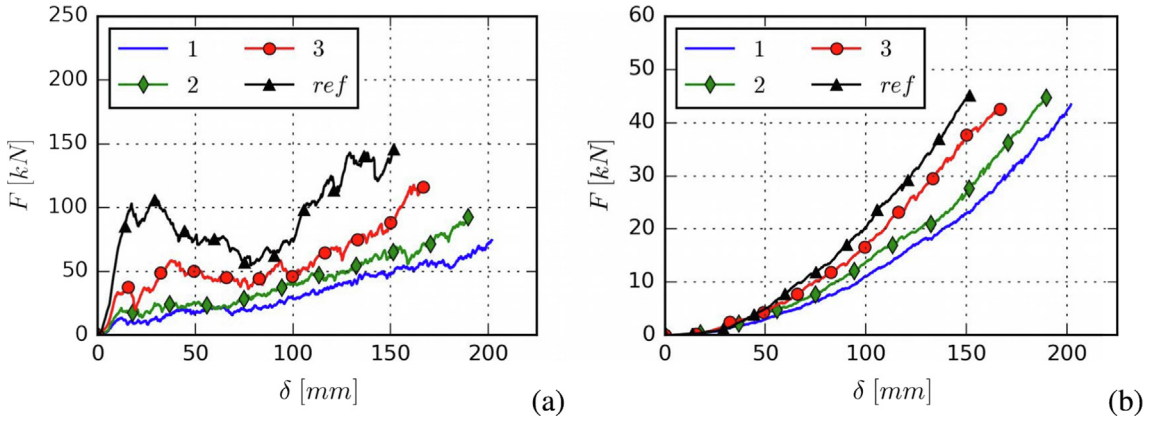

Fig. 21. Comparison of the mechanical response of (a) the overall system and (b) the solely mesh obtained for different soil types.

constraint imposed to the mesh z-displacement for less frictional soils.

This simple analysis has highlighted that the force–displacement behavior of the soil-mesh-plate system, as well as its ultimate bearing capacity are strongly affected by the soil type. Therefore, it is recommended to consider soil layers of different mechanical properties in the experimental characterization. In the same way, it could be inferred that the soil porosity may also play an important role with the appearance of a peak failure for dense dilating soils and the absence of the peak for loose soils like in the classic foundation engineering (Budhu, 2010).

5.3.3. Effect of the anchor plate size

The effect of the plate size b on the response of the system is analyzed by changing its value in the range 150 mm $\leqslant b \leqslant$ 400 mm. The obtained results are shown in Fig. 22. The adoption of a larger plate leads to an increase of both the soil bearing capacity (f_S) and the mesh maximum puncturing force (f_M). The former was estimated as the peak force value in the first phase of the test and is highlighted with a star marker in Fig. 22a. It should be noted that for large anchor plates the system shows a "fragile" mechanical response, its bearing capacity being reached for a relatively low displacement of the plate (i.e. before activating the mesh response, see the case $b = 400$ mm in Fig. 22a). Conversely, a "ductile" behavior is observed for a relatively small plate size for which the bearing capacity is reached at large displacements (see the case $b = 250$ mm in Fig. 22a). In the former case, the ultimate bearing capacity is controlled by the soil strength only, while in the latter it is given by the combined resistance of both the soil and the mesh. In the configuration here considered, the threshold plate dimension that determines

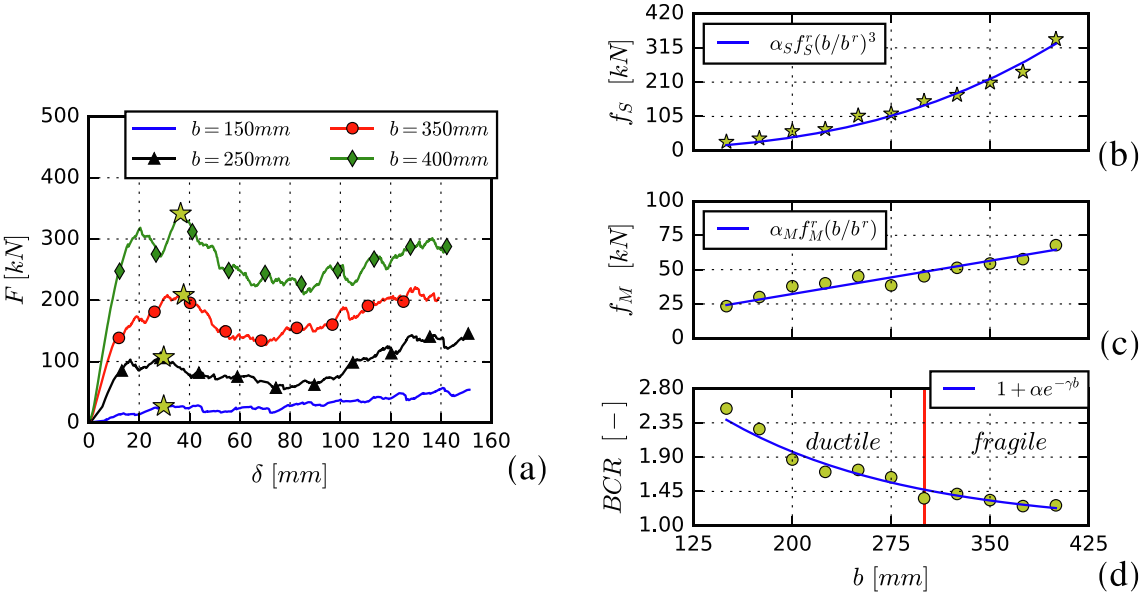

Fig. 22. Effect of the anchor plate size. (a) Comparison of the system mechanical behavior obtained by considering a different size of the plate. (b) Soil "bearing capacity" with the presence of the mesh (f_S), (c) mesh puncturing resistance (f_M) and (d) bearing capacity ratio (BCR) as a function of the plate side dimension.

the transition between a "fragile" and a "ductile" behavior can be identified as a plate side $b = 300$ mm; nevertheless, this critical value depends on both the soil and the mesh mechanical properties and therefore should not considered as a reference value.

The trends of the two contributions f_S and f_M as a function of b are reported in Fig. 22b and Fig. 22c respectively. Firstly, it can be observed that the estimated soil bearing capacity, obtained with the presence of the mesh panel, is well fitted by a cubic function of b ($f_S = \alpha_S f_S^r \left(\frac{b}{b^r}\right)^3$, with $\alpha_S = 0.75$ and f_S^r indicating the reference case $b^r = 250$ mm). A punch test without the presence of the mesh panel is also performed for each of the values of b previously considered and a cubic relation between the bearing capacity and the plate dimension is found also in this case. This result is in perfect agreement with the classical theory of shallow foundations (Terzaghi and Peck, 1967). On the other hand, the ultimate puncturing force of the mesh (see Fig. 22c) linearly scales with the plate dimension ($f_M = \alpha_M f_M^r \frac{b}{b^r}$, with $\alpha_M = 0.89$ and f_M^r indicating the reference case $b^r = 250$). The puncturing resistance of the mesh is, in fact, governed by the number of wires intercepted by the punching element and linearly scales with the plate side; this result is in agreement with what has been observed in Pol, (2020) and Pol et al., (2021b).

Finally, the influence of the anchor plate size b on the bearing capacity ratio is considered. It is useful to recall that the BCR is here computed as the ratio between the maximum force registered during the test with the presence of the mesh over the one related to the case without the mesh, for a given value of the plate side b. The thus obtained BCR values are reported in Fig. 22d as a function of the plate side. From the fit of the numerical data, it is notable that the BCR shows an exponential decay with the anchor plate size ($BCR = 1 + \alpha e^{-\gamma b}$, with $\alpha = 4.07$ and $\gamma = 7.2 \times 10^{-3}$ mm^{-1}). This highlights that the benefit in the system resistance, related to the introduction of the mesh, is significant when a plate of relatively small dimension is adopted ($BCR \geqslant 1.5$ for $b \leq 275$ mm), while it is strongly reduced for large values of plate size. Furthermore, it can be observed that the introduction of the mesh efficiently increases the ultimate bearing capacity of the system when its response is characterized by a "ductile" behavior, while for a "fragile" behavior the gain in terms of BCR provided by the mesh insertion is very low.

6. Conclusions

In this work, the mechanical behavior of flexible mesh facings was investigated starting from experimental results obtained in a special plate bearing capacity test configuration. This configuration is intended to mimic the local interaction mechanism between the flexible mesh facing and the underlying soil layer, taking place at the level of the anchored zones of the system.

A 3D discrete element approach was adopted in order to reproduce the experimental results. A model of the punch against soil test was calibrated on the basis of experimental data. The numerical simulations allowed an in-depth analysis of the nontrivial interaction mechanism between the wire mesh, the anchor plate and the underlying granular layer. The mechanical behavior of the soil-mesh-plate system can be characterized as a three-steps process. Firstly, for low displacements, the response of the system is controlled by the soil mechanical response. Secondly, in the intermediate step of the test, the pure mechanical contribution of the mesh in contrasting the plate displacement is still negligible, but it actively interacts with the soil preventing the full development of a failure mechanism in the soil layer. Thirdly, for a displacement level that is sufficiently large to tension the mesh, the mesh imposes an active contrast to the plate displacement as well as a confining pressure on the soil layer. These contributions progressively increase with the plate displacement until the failure of the mesh is reached. It was observed that the presence of the mesh determines a lateral shift of the soil emerging zones and a deepening of the failure surface in the soil layer. In this perspective, the effect of the mesh can be seen as an enlargement of the "effective footprint" of the anchor plate. Finally, a parametric analysis aimed at quantifying the role of the problem's variables on the system response was performed. The main results are summarized as follows:

- **the mesh mechanical properties** have shown to play a significant role on the soil-mesh-plate mechanical behavior. A large increase of the bearing capacity of the soil-mesh-plate system was observed when improving the mechanical properties of the mesh panel; only in a minor way was this due to the higher puncturing resistance of the mesh, while the major contribution was provided by the enhancement of the mesh-soil interaction;
- **the soil mechanical properties** have a nontrivial effect on the mechanical response. This highlights the importance of using different soil typologies in the experimental characterization;
- **the anchor size** strongly influences the mechanical response as well as the bearing capacity of the system. The bearing capacity ratio shows an exponential decay with the anchor plate size and may become negligible for large anchor plates. Furthermore, it was found that a critical plate dimension exists that determines the transition between a "ductile" and a "fragile" behavior of the system.

The results presented in this work have permitted an in-depth analysis of the local interaction mechanism taking place at the level of the anchor plates of an flexible mesh facing from laboratory to idealized field conditions. However, it should be noted that this work represents a first step in the understanding of the variables that control the response of an anchored mesh system in "real" field condi-

tions. Further information on the extension to the field conditions can be found in Pol and Gabrieli (2021). Moreover, this study has shown the potential of a 3D discrete element approach for characterizing the relation between the local contrast at the level of the anchor plates and the relative movements of the underlying soil mass. This methodology may therefore represent an useful tool for the definition of the so-called "characteristic curve", which is at the base of a recently proposed "hybrid" design approach for anchored wire meshes (Galli et al., 2020; Officine Maccaferri S.p.A, 2021) and a key point to move towards a full displacement-based design approach.

Acknowledgement

This work was supported by the Research Grant awarded to A. Pol by the University of Padova. The authors acknowledge the financial support of Cariverona R&S 2018, MIUR (Redreef - PRIN 2017 Call, prot. 2017YPMBWJ). The authors would like to acknowledge Maccaferri Innovation Center for the experimental data.

References

Albaba, A., Lambert, S., Kneib, F., Chareyre, B., Nicot, F., 2017. DEM Modeling of a Flexible Barrier Impacted by a Dry Granular Flow. Rock Mech. Rock Eng. 50, 3029–3048. https://doi.org/10.1007/s00603-017-1286-z.

Andreotti, B., Forterre, Y., Pouliquen, O., 2013. Granular Media: Between Fluid and Solid. Cambridge University Press.

Belheine, N., Plassiard, J.P., Donzé, F.V., Darve, F., Seridi, A., 2009. Numerical simulation of drained triaxial test using 3d discrete element modeling. Comput. Geotech. 36, 320–331. https://doi.org/10.1016/j.compgeo.2008.02.003.

Bergado, D., Teerawattanasuk, C., Long, P., 2000. Localized mobilization of reinforcement force and its direction at the vicinity of failure surface. Geotext. Geomembr. 18, 311–331. https://doi.org/10.1016/S0266-1144(99)00033-3.

Bergado, D.T., Teerawattanasuk, C., 2008. 2d and 3d numerical simulations of reinforced embankments on soft ground. Geotext. Geomembr. 26, 39–55. https://doi.org/10.1016/j.geotexmem.2007.03.003.

Bertrand, D., Nicot, F., Gotteland, P., Lambert, S., 2005. Modelling a geo-composite cell using discrete analysis. Comput. Geotech. 32, 564–577. https://doi.org/10.1016/j.compgeo.2005.11.004.

Bertrand, D., Nicot, F., Gotteland, P., Lambert, S., 2008. Discrete element method (DEM) numerical modeling of double-twisted hexagonal mesh. Can. Geotech. J. 45, 1104–1117. https://doi.org/10.1139/T08-036.

Boschi, K., di Prisco, C., Flessati, L., Mazzon, N., 2021. Numerical analysis of the mechanical response of anchored wire meshes. In: Barla, M., Di Donna, A., Sterpi, D. (Eds.), Challenges and Innovations in Geomechanics. Springer International Publishing, pp. 779–785.

Budhu, M., 2010. Soil Mechanics and Foundations, 3rd ed. John Wiley & Sons Ltd..

Calvetti, F., Nova, R., 2004. Micromechanical approach to slope stability analysis. In: Darve, F., Vardoulakis, I. (Eds.), Degradations and Instabilities in Geomaterials. Springer, Vienna, pp. 235–254.

Calvetti, F., di Prisco, C., Nova, R., 2004. Experimental and numerical analysis of soil-pipe interaction. J. Geotechn. Geoenviron. Eng. 130, 1292–1299. https://doi.org/10.1061/(ASCE)1090-0241(2004)130:12(1292).

Calvetti, F., Viggiani, G., Tamagnini, C., 2003. A numerical investigation of the incremental behavior of granular soils. Rivista Italiana di Geotecnica 3, 11–29.

Cheng, H., Shuku, T., Thoeni, K., Yamamoto, H., 2018. Probabilistic calibration of discrete element simulations using the sequential quasi-monte carlo filter. Granular Matter 20, 11. https://doi.org/10.1007/s10035-017-0781-y.

Ciantia, M.O., Arroyo, M., Butlanska, J., Gens, A., 2016. Dem modelling of cone penetration tests in a double-porosity crushable granular material. Comput. Geotech. 73, 109–127. https://doi.org/10.1016/j.compgeo.2015.12.001.

Coulibaly, J.B., Chanut, M.A., Lambert, S., Nicot, F., 2017. Nonlinear Discrete Mechanical Model of Steel Rings. J. Eng. Mech. 143. https://doi.org/10.1061/(ASCE)EM.1943-7889.0001303.

Cundall, P.A., Strack, O.D.L., 1979. A discrete numerical model for granular assemblies. Géotechnique 29, 47–65. https://doi.org/10.1680/geot.1979.29.1.47.

Ferraiolo, F., Giacchetti, G., 2004. Rivestimenti corticali: alcune considerazioni sull'applicazione delle reti di protezione in parete rocciosa. Atti del convegno Bonifica dei versanto rocciosi per la protezione del territorio, 147–176.

Gabrieli, F., Cola, S., Calvetti, F., 2009. Use of an up-scaled dem model for analysing the behaviour of a shallow foundation on a model slope. Geomech. Geoeng. 4, 109–122. https://doi.org/10.1080/17486020902855688.

Gabrieli, F., Pol, A., Mazzon, N., Deana, M.L., 2020. Discrete element simulations of punch tests for the mechanical characterization of cortical meshes. In: da Fontoura, S.A., Jose Rocca, R., Mendoza, J.P. (Eds.), Rock Mechanics for Natural Resources and Infrastructure Development. CRC Press, London, pp. 3401–3407.

Gabrieli, F., Pol, A., Thoeni, K., 2017. Comparison of two DEM strategies for modelling cortical meshes. Proc. Particle-based Methods - Fund. Appl. Particles 2017, 489–496.

Gabrieli, F., Pol, A., Thoeni, K., Mazzon, N., 2018. Particle-based modelling of cortical meshes for soil retaining applications. Numerical Methods in Geotechnical Engineering IX. CRC Press, London, pp. 391–397.

Galli, A., Deana, M.L., Mazzon, N., 2020. Application of a hybrid approach to the design of anchored wire meshes on steep slopes. In: Proceedings of the 2020 International Symposium on Slope Stability in Open Pit Mining and Civil Engineering, Australian Centre for Geomechanics. pp. 823–830. https://doi.org/10.36487/ACG_repo/2025_53.

Galli, A., Maiorano, R.M.S., di Prisco, C.G., Aversa, S., 2017. Design of slope-stabilizing piles: from ultimate limit state approaches to displacement based methods. Rivista Italiana di Geotecnica 51, 77–93.

Galli, A., di Prisco, C.G., 2013. Displacement-based design procedure for slope-stabilizing piles. Can. Geotech. J. 50, 41–53. https://doi.org/10.1139/cgj-2012-0104.

Iwashita, K., Oda, M., 1998. Rolling resistance at contacts in simulation of shear band development by dem. J. Eng. Mech.s 124, 285–292. https://doi.org/10.1061/(ASCE)0733-9399(1998)124:3(285).

Li, X., Zhao, J., 2018. A unified cfd-dem approach for modeling of debris flow impacts on flexible barriers. Int. J. Numer. Anal. Meth. Geomech. 42, 1643–1670. https://doi.org/10.1002/nag.2806.

Marigo, N., Gabrieli, F., Pol, A., Bisson, A., Brezzi, L., 2021. A discrete element framework for the modelling of rock-filled gabions. IOP Conf. Series: Earth Environ. Sci. 833, 012102. https://doi.org/10.1088/1755-1315/833/1/012102.

McDowell, G.R., Harireche, O., Konietzky, H., Brown, S.F., Thom, N. H., 2006. Discrete element modelling of geogrid-reinforced aggregates. Proc. Inst. Civil Eng.- Geotech. Eng. 159, 35–48. https://doi.org/10.1680/geng.2006.159.1.35.

Muhunthan, B., Shu, S., Sasiharan, N., Hattamleh, O.A., 2005. Analysis and design of wire mesh/cable net slope protection. Technical Report. Washington State Transportation Commission Department of Transportation.

Officine Maccaferri S.p.A, 2021. Mac S-Design - Scientific Manual.

Plassiard, J.P., Belheine, N., Donze, F., 2009. A spherical discrete element model: Calibration procedure and incremental response. Granular Matter 11, 293–306. https://doi.org/10.1007/s10035-009-0130-x.

Pol, A., 2020. Discrete element modelling of wire meshes for secured drapery applications. Ph.D. thesis. Universitá degli Studi di Padova.

Pol, A., Gabrieli, F., 2021. Discrete element simulation of wire-mesh retaining systems: An insight into the mechanical behaviour. Comp. Geotech. 134. https://doi.org/10.1016/j.compgeo.2021.104076.

Pol, A., Gabrieli, F., Bost, M., 2021a. A simple tool for forecasting the mechanical response of anchored wire mesh panels. IOP Conf. Series: Earth Environ. Sci. 833, 012104. https://doi.org/10.1088/1755-1315/833/1/012104.

Pol, A., Gabrieli, F., Brezzi, L., 2021b. Discrete element analysis of the punching behaviour of a secured drapery system: from laboratory characterization to idealized in situ conditions. Acta Geotech. https://doi.org/10.1007/s11440-020-01119-z.

Pol, A., Gabrieli, F., Mazzon, N., 2020. Enhancement of Design Methodologies of Anchored Mesh Systems Using the Discrete Element Method. In: Geotechnical Research for Land Protection and Development, Springer International Publishing. pp. 500–508. https://doi.org/10.1007/978-3-030-21359-6_53.

di Prisco, C.G., Besseghini, F., Pisanò, F., 2010. Modelling of the mechanical interaction between anchored wire meshes and granular soils. Geomech. Geoeng. 5, 137–152. https://doi.org/10.1080/17486020903576218.

Sibille, L., Nicot, F., Donzé, F.V., Darve, F., 2007. Material instability in granular assemblies from fundamentally different models. Int. J. Numer. Anal. Meth. Geomech. 31, 457–481. https://doi.org/10.1002/nag.591.

Smilauer, V., Angelidakis, V., Catalano, E., Caulk, R., Chareyre, B., et al., 2021. Yade documentation. The Yade Project. https://doi.org/10.5281/zenodo.5705394.

Terzaghi, K., Peck, R.B., 1967. Soil Mechanics in Engineering Practice. John Wiley.

Thoeni, K., Giacomini, A., Lambert, C., Sloan, S.W., Carter, J.P., 2014. A 3D discrete element modelling approach for rockfall analysis with drapery systems. Int. J. Rock Mech. Min. Sci. 68, 107–119. https://doi.org/10.1016/j.ijrmms.2014.02.008.

Thoeni, K., Lambert, C., Giacomini, A., Sloan, S.W., 2013. Discrete modelling of hexagonal wire meshes with a stochastically distorted contact model. Comput. Geotech. 49, 158–169. https://doi.org/10.1016/j.compgeo.2012.10.014.

UNI 11437, 2012. Rockfall protective measures - tests on meshes for slopes coverage.

Volkwein, A., Schellenberg, K., Labiouse, V., Agliardi, F., Berger, F., Bourrier, F., Dorren, L.K.A., Gerber, W., Jaboyedoff, M., 2011. Rockfall characterisation and structural protection – a review. Natural Hazards Earth Syst. Sci. 11, 2617–2651. https://doi.org/10.5194/nhess-11-2617-2011.

Wensrich, C., Katterfeld, A., 2012. Rolling friction as a technique for modelling particle shape in dem. Powder Technol. 217, 409–417. https://doi.org/10.1016/j.powtec.2011.10.057.